Testing, characterization, and control of a multi-axis, high precision drive system for the Hobby-Eberly Telescope Wide Field Upgrade

Soukup, Ian, Beno, Joseph, Hill, Gary, Good, John, Penney, Charles, et al.

Ian M. Soukup, Joseph H. Beno, Gary J. Hill, John M. Good, Charles E. Penney, Timothy A. Beets, Jorge D. Esguerra, Richard J. Hayes, James T. Heisler, Joseph J. Zierer, Gregory A. Wedeking, Michael S. Worthington, Douglas R. Wardell, John A. Booth, Mark E. Cornell, Marc D. Rafal, "Testing, characterization, and control of a multi-axis, high precision drive system for the Hobby-Eberly Telescope Wide Field Upgrade," Proc. SPIE 8444, Ground-based and Airborne Telescopes IV, 84443X (17 September 2012); doi: 10.1117/12.926389

SPIE.

Event: SPIE Astronomical Telescopes + Instrumentation, 2012, Amsterdam, Netherlands

Testing, characterization, and control of a multi-axis, high precision drive system for the Hobby-Eberly Telescope Wide Field Upgrade

Ian M. Soukup[b], Joseph H. Beno[b], Gary J. Hill[a], John M. Good[a], Charles E. Penny[b], Timothy A. Beets[b], Jorge D. Esguerra[b], Richard J. Hayes[b], James T. Heisler[b], Joseph J. Zierer[b], Gregory A. Wedeking[b], Michael S. Worthington[b], Douglas R. Wardell[b], John A. Booth[a], Mark E. Cornell[a], Marc D. Rafal[a]

[a]The University of Texas McDonald Observatory, 1 University Station C1402, Austin, Texas, USA 78712-0259
[b]The University of Texas Center for Electromechanics, 1 University Station R7000, Austin, Texas USA 78712

ABSTRACT

A multi-axis, high precision drive system has been designed and developed for the Wide Field Upgrade to the Hobby-Eberly Telescope at McDonald Observatory. Design, performance and controls details will be of interest to designers of large scale, high precision robotic motion devices. The drive system positions the 20-ton star tracker to a precision of less than 5 microns along each axis and is capable of 4 meters of X/Y travel, 0.3 meters of hexapod actuator travel, and 46 degrees of rho rotation. The positioning accuracy of the new drive system is achieved through the use of high-precision drive hardware in addition to a meticulously tuned high-precision controller. A comprehensive understanding of the drive structure, disturbances, and drive behavior was necessary to develop the high-precision controller. Thorough testing has characterized manufacture defects, structural deflections, sensor error, and other parametric uncertainty. Positioning control through predictive algorithms that analytically compensate for measured disturbances has been developed as a result of drive testing and characterization. The drive structure and drive dynamics are described as well as key results discovered from testing and modeling. Controller techniques and development of the predictive algorithms are discussed. Performance results are included, illustrating recent performance of several axes of the drive system. This paper describes testing that occurred at the Center for Electromechanics in Austin Texas.

Keywords: Center for Electromechanics, CEM, Hobby-Eberly Telescope, HET, HETDEX, University of Texas, McDonald Observatory, Telescope tracking systems, Large hexapod positioning systems, High payload hexapod positioning systems, precision positioning systems, hexapod design and controls

1. INTRODUCTION

The Hobby Eberly Telescope, designed to gather large amounts of light for spectroscopy, is undergoing a transformation to begin the search for "Dark Energy". Dark energy is a term used to describe unknown forces causing the acceleration of cosmic expansion[1,2]. To help define the evolution and significant properties of dark energy, the Hobby Eberly Telescope (HET) at the McDonald Observatory (MDO) was chosen to survey and map the locations of other galaxies in space. This Dark Energy Experiment (DEX), which is estimated to be completed over 100 nights of viewing, is now referred to as HETDEX[3]. The success of HETDEX is highly dependent on the dynamic positioning performance of the upgraded telescope tracking system. Disturbances, noise, drive structure uncertainties and random drive behavior can all contribute to performance degradation. The HETDEX tracker has the added complexity of positioning a large payload, 20 tons, and traversing a large range or travel: 4 meters of X/Y travel, 0.3 meters of hexapod actuator travel, and 46 degrees of rho rotation[4]. The controller development focused on system identification and error compensation that evolved from extensive testing. The testing followed a laddered approach where root level tuning and error compensation algorithms were implemented first through individual actuator or independent axis testing, followed by progressive grouping of subsystems or elements. This approach created layered error compensation algorithms that were executed serially during motion control. Two parallel test paths were implemented in order to reduce overall schedule length; one test path focused on the X/Y system, while the other focused on the hexapod, **Figure 1** and **Figure 2**. Examples of tuning, error compensation algorithms, system identification, and other significant test results will be discussed for each subsystem.

Ground-based and Airborne Telescopes IV, edited by Larry M. Stepp, Roberto Gilmozzi, Helen J. Hall,
Proc. of SPIE Vol. 8444, 84443X · © 2012 SPIE · CCC code: 0277-786/12/$18 · doi: 10.1117/12.926389

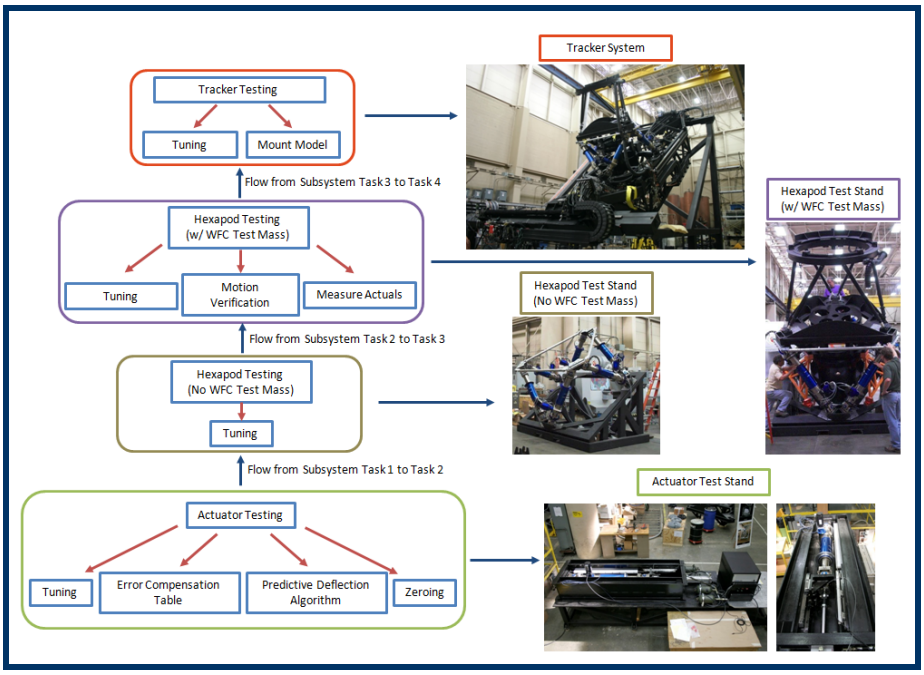

Figure 1. Hexapod Testing Flow Chart – The chart plots the upward progression from single actuator testing to the fully assembled tracker testing phase.

The images illustrate the flow of testing from the more basic subsystems to the fully assembled system. The lowest subsystems highlighted in the green boxes were the initial test cases for the hexapod and X/Y systems. The tests progressed for each system until the tracker was fully assembled; at which time the two paths merged to begin the "Tracker Testing" phase. Each subsystem test is identified as a sequentially number "Task" in Figure 1 and Figure 2. The "Tasks" contain the identifier for each test phase (e.g. "Actuator Testing") followed by the achievements, identified by the red arrows, that flowed from the completion of one task to the start of another.

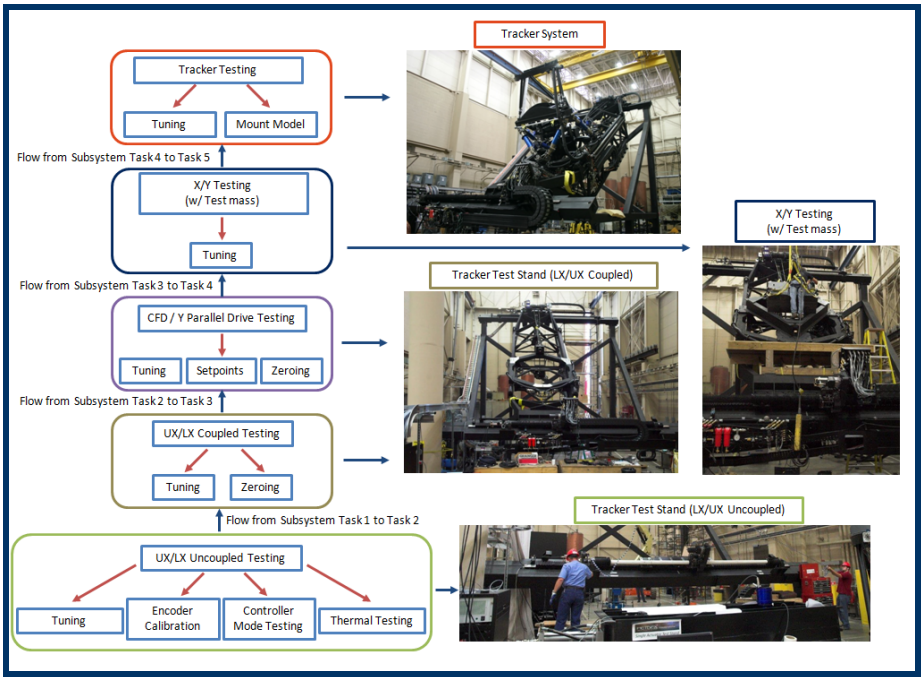

Figure 2. X/Y System Testing Flow Chart – These tests progressed in parallel with the hexapod testing to reduce schedule length

2. HEXAPOD TESTING

The hexapod actuators underwent extensive testing via a single actuator test stand. The single actuator test stand was configurable to apply four loading conditions to the actuators representing their fully assembled load states: 17-25kN compression, 4-7 kN compression, 3-5 kN tension and no load[5]. The single actuator test stand provided an ideal test space for charactering each actuator in an isolated environment. Major accomplishments include 1) actuator performance tuning and 2) implementation of sensor error correction tables and algorithms.

2.1 Actuator Tuning and Performance – Single Actuator Test Stand

The hexapod actuator controller used a position to velocity cascaded control loop with a 1 kHz controller cycle time. The Danaher Motion AC servo drives were programmed to torque mode resulting in analog current commands being sent to each actuator motor. Feedback was obtained from an absolute Heidenhain EnDAT encoder with 32 bit resolution and 0.5 micron accuracy grade[6]. Controller gain tuning was performed on each actuator resulting in 0.75 to 1 microns RMS "following error" at 1 mm/s as measured by the dSPACE controller hardware, Figure 3. "Following error" is defined as the command position subtracted from the sensor position for each control cycle.

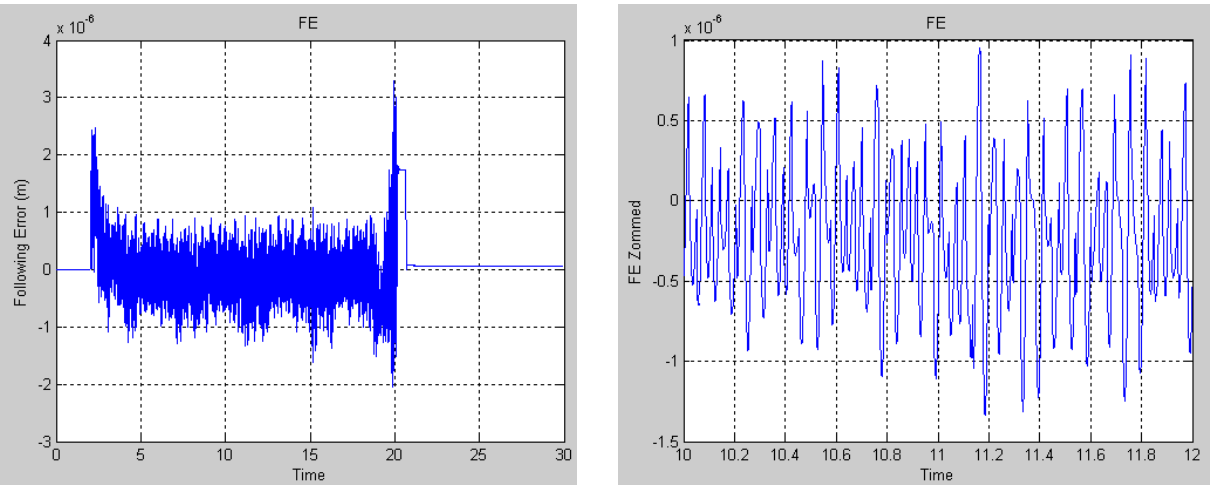

Figure 3. The plots illustrate actuator following error measurements made by the dSPACE controller. These plots were recorded from an actuator that was undergoing testing in the single actuator test stand.

2.2 Zeroing, Error Compensation, and Predictive Deflection Algorithms – Single Actuator Test Stand

Calibration of the actuator feedback device, Heidenhain encoder, began by defining the zero positions of each actuator. This was achieved by measuring the distance between the pin locations in our solid model for the actuators at their home position and comparing this to the pin distance measurements made by an API laser tracker for each actuator in the test stand. The difference between the model and the actual measurements generated the offsets that were applied to each actuator sensor. Limit switch positions were located and adjusted to design specifications as needed once the actuators' zero positions were defined.

Error compensation tables were developed for each actuator to adjust for sensor error as a function of actuator displacement. It was determined that in order to achieve the highest accuracy measurements from the laser tracker, precise alignment of the laser tracker to the actuator's axis of motion was required. This minimized the use of the encoders in the laser tracker and therefore the distance calculated by the laser tracker became largely a function of interferometry only. Sensor data and laser data was gathered by moving the actuator from one end of travel to the other (totaled 295 mm) while pausing every 1mm. During the pauses, measurements were automatically made and recorded by both the laser tracker and the dSPACE controller hardware. These measurements were repeated for each actuator at each load condition. Data from the measurements was used to calculate the error associated with the encoders as defined in equation 1.

$$error = laser - encoder \tag{1}$$

Error plots were generated as a function of actuator displacement for each load case, **Figure 4**. Repeatability was examined by taking several data sets for each load condition as shown in **Figure 4**.

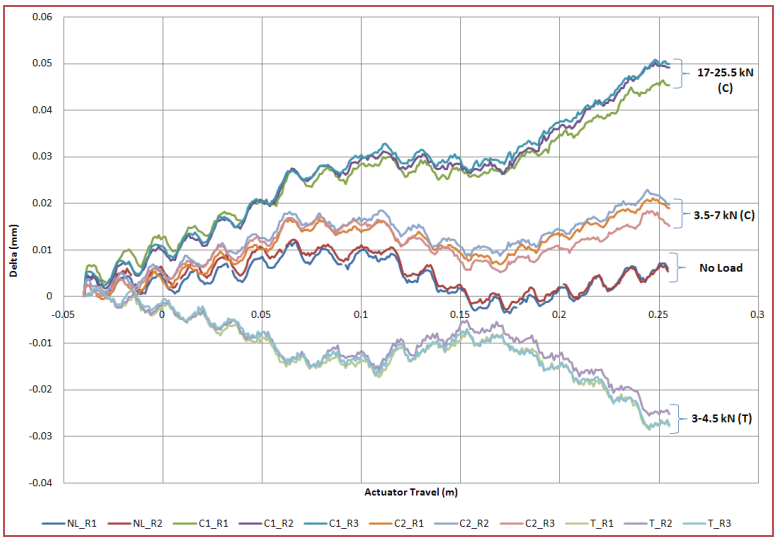

Figure 4. Actuator sensor error was recorded as illustrated in this figure for each load condition. Multiple runs are shown for repeatability verification.

The data shows very similar characteristics for each load case and confirms a high level of repeatability. By inspection each error curve demonstrated a low frequency roll with a superimposed higher frequency oscillation. The other imperative observation is that the slope of the data sets for each load condition is a function of actuator deflection. Deflection occurred due to the mechanical stiffness of the actuator reflecting the increase in load from one end of travel to the other.

Two methods of error compensation were evaluated to correct for the encoder error. 1) A 6th order polynomial curve fit with superimposed sine wave was generated, which resulted in a maximum 13 microns of error when measured against the averaged no load data sets. 2) A linear correction table function, 1-D lookup table generated in SimuLink, resulted in a maximum 6 microns of error when measured against the averaged no load data sets. Based on improved matching the 1-D lookup table was chosen over the polynomial curve fit.

Predictive deflection algorithms were developed in order to eliminate the error associated with the deflection due to mechanical stiffness. The stiffness of each actuator was calculated from the slope of the error curves in **Figure 5**; the delta was calculated using equation 2.

$$\delta = \frac{\Delta F}{k_{act}} \tag{2}$$

The delta function was subtracted from the error curves, for each load case, resulting in a rotational shift of the curves so that the loaded conditions matched the no load condition, **Figure 5**.

The measured error, red line, is first shifted using the predictive stiffness algorithm which generated the blue line. The purple line is a no-load error measurement and shows a close match to the shifted curve; the purple line is for illustrative purposes and was used to generate the linear correction table. Next the linear correction table function takes the data from the blue line and generates the orange line, which is the final corrected error curve of the sensor. The error was reduced from over 40 microns to less than 5 microns.

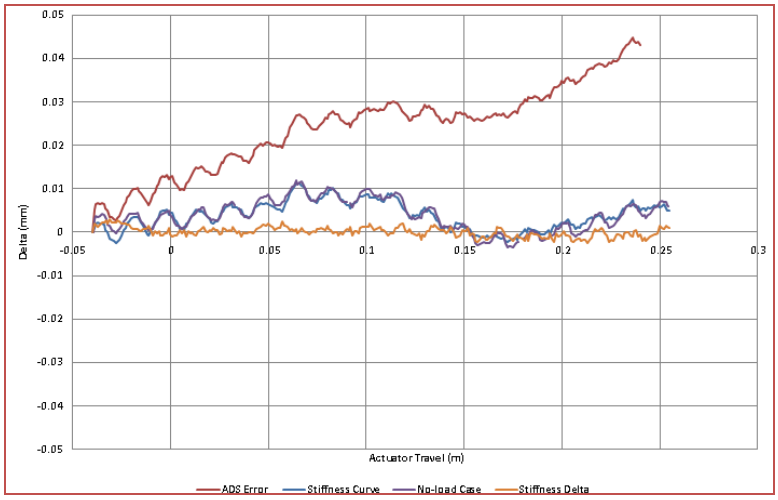

Figure 5. Shown is an example of a stiffness correction applied to the red line to generate the blue line The linear correction table then generates the orange line.

2.3 Tuning, Measuring Actuals, and Motion Verification – Hexapod Test Stand

The hexapod was assembled onto the hexapod test stand, shown in **Figure 6**, with the addition of a Wide Field Corrector [WFC] test mass that had similar inertial and geometric properties to the new WFC[5]. The hexapod test stand not only enabled parallel testing of the X/Y system but provided a more manageable environment for testing and measuring.

Measurement features swept by the laser tracker were much more accessible in the test stand and therefore prevented fabrication of special tooling that would be required for making measurements with the hexapod installed on the tracker. Hexapod testing accomplished the following: performance tuning, motion verification, and measurement of as-built geometry (e.g. U-Joint Rotation Centers, Upper / Lower U-Joint Planes, and Upper / Lower U-joint Circle Centers).

"Following error" plots similar to **Figure 3** were generated for each actuator with command velocities ranging from 0.05mm/s to 3mm/s. The controller gains for the actuators were tweaked until the following error performance was less than 3 micron RMS for each actuator.

The laser tracker measured the rotation centers of the actuators, defined the two planes located at the upper and lower U-Joint centers, and positioned targets at the predicted WFC Control Point and Stationary-Image Rotation Point [SIRP]. These measurements generated new actuator offsets that replaced the original actuator offsets defining the actuator zero position. The locations of the U-Joint centers and U-Joint planes were entered into the hexapod motion controller so that the calculated actuator lengths based on the orientation of the upper-U joint plane would have higher fidelity.

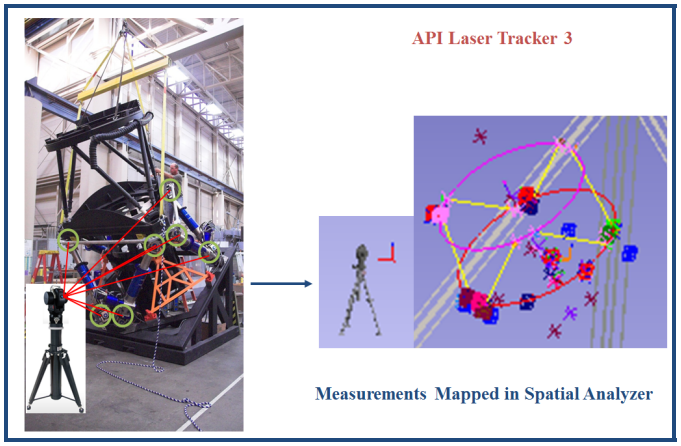

Figure 6. The images illustrate measurement points with the API Laser Tracker 3 and recording the points in Spatial Analyzer. With hexapod conveniently located on the hexapod test stand over two dozen features were measured to accurately define as built geometry and predict the WFC control point and SIRP.

Motion verification tests were performed to verify that motion control algorithms calculated valid commands and that the desired motion envelope was within the mechanical limitations of hexapod components. According to calculations there were six pre-determined conditions that resulted in the largest U-Joint articulation. These conditions were calculated through an iterative parametric analysis that utilized hexapod SolidWorks models and calculated component motion[7]. The six conditions were tested and visual inspection concluded that the U-Joint articulation abilities were more than adequate to achieve the desired motion envelope. To validate the motion control algorithms the laser tracker was used to measure the position of the hexapod given an X,Y,Z,Theta,Phi command. Measurement targets were strategically located to provide translation and rotation results of the WFC test mass SIRP. Initial tests indicated a delta of less than 20 arc seconds between the laser and the dSPACE command.

3. X/Y SYSTEM TESTING

X/Y independent testing was critical in discovering controller weaknesses, feedback sensor limitations, structural resonances, temperature dependences, torque requirements, and load sharing characteristics of the Y/CFD parallel drive operation. These tests drove design changes for the controller, feedback sensors, motor/gearhead combinations, grease lubrication, and defined the parallel drive set points.

3.1 Initial Testing and Tuning

Initial installation of the X/Y system required setting the linear encoders for each axis and calibrating the tape tension to achieve the desired X/Y position feedback accuracy from the encoder. This was accomplished by mounting the laser tracker so that it measured along the axis of motion; each axis was tensioned independently with different laser setups (i.e. 3 setups were required: lower X [LX], upper X [UX], and Y). The X axis trolleys and Y axis carriage were positioned from positive stop to negative stop; encoder measurements were recorded by the dSPACE controller and laser

tracker measurements were recorded at each stop. The tape tension was adjusted for each axis until the measurements reported by the dSPACE controller were within 10 microns of the laser tracker readings.

At first the X axis controller used a position to velocity cascaded control loop with a 1 kHz controller cycle time similar to the controller for the hexapod actuators[6]. The Danaher Motion AC servo drives were programmed to torque mode resulting in analog current commands being sent to each actuator motor. Feedback was obtained from an incremental Heidenhain linear encoder with 0.3 micron resolution and +/- 5 micron accuracy grade. It was quickly determined that the following error for the Upper X axis [UX] and Lower X axis [LX] was substantially larger, measuring 15 to 20 um peak to peak, than the measurements for the hexapod, **Figure 7**.

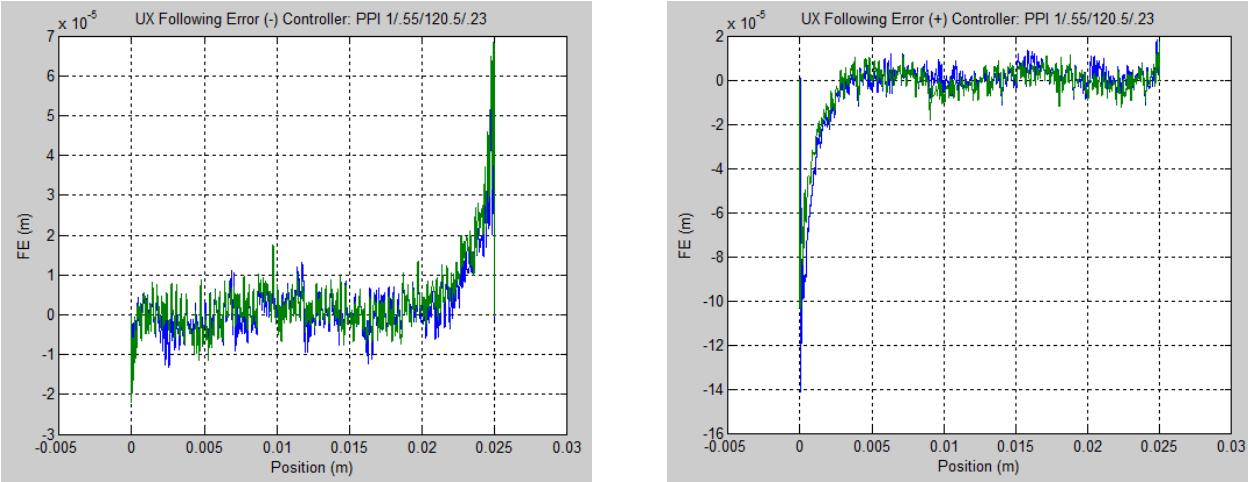

Figure 7. UX/LX Following error plots in torque mode show larger following error than what was achieved by the hexapod actuators.

Testing indicated that the larger following error was a result of decreased system bandwidth due to the following factors: reduced system stiffness, lower feedback resolution, and noisier feedback sensors. To address these issues the LX/UX and Y servo drives were configured to operate in velocity mode. A stiffer dynamic system was produced by allowing the drive to use feedback from a sensor at the back of the motor for velocity control while the linear encoder at the other end of the drive system closed only the position loop. To further enhance the controller performance motors with digital Heidenhain encoders were used to replace the existing motors that had resolver feedback. The new sensor improved sensor resolution and reduced sensor noise producing a better performing controller. The following error performance increased by a factor of two, reducing the error from 15-20 microns to less than 10 microns, **Figure 8**.

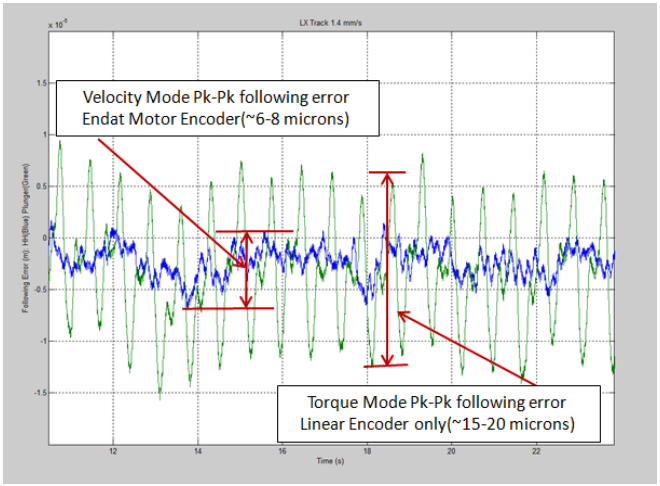

Figure 8. Image shows the increased performance with velocity control and Heidenhain digital motor encoders. The blue line illustrates the new performance with only 6-8 micron peak to peak as compared to the original following error traced by the green line.

3.2 Constant Force Drive/Y Drive Parallel Testing

Testing and tuning the parallel drive systems, Y drive and Constant Force Drive [CFD], was also performed before the tracker assembly was completed. The CFD operates as the active safety system for the tracker while the Y drive positions the SIRP along the Y axis of the primary mirror[8]. The CFD employs an analog controller to represent Proportional Integral Derivative [PID] control to the wire rope tension based on load cell feedback[8]. The Y drive is controlled with the equivalent control method as described for the X axes. It was determined that there was a delicate balance between the control shared by these two systems. Several scenarios were tested: 1) open loop CFD control that provided constant current to the CFD drive 2) high load percentage carried by the CFD with PID control and 3) low load percentage carried by the CFD with PID control. Testing showed that running the CFD with open loop constant current control generated very large spikes in following error. Although the motor received a constant current command the force felt by the carriage and Y-drive was erratic. It is believed that the force felt by the Y-drive varied due to the following two reasons:

- Stiction - the CFD is a large drive system including the largest Danaher AKM series servo motor, AKM74P, a hefty industrial 140:1 reduction bevel-helical gearbox (Renold Brand HC Series), as well as a large 10 inch diameter steel drum with overhead lift rated bearing units
- Inertia- the large system also possesses high rotational inertia which resulted in fluctuating inertial forces as the carriage accelerated to constant speed.

After discovering the inability to operate the CFD with open loop control, tests were conducted to determine the influences on performance while operating the CFD under PID control. Of particular interest was the relationship between CFD load set point and following error performance. Based on following error performance plots, the higher the load carried by the CFD the more it adversely influenced the Y-Drive performance. The higher load cases gave the CFD more force authority causing its control loop to overpower the Y-Drive controller and produced increased following error disturbances. At low set points the CFD still maintains all of its safety functionality, assuming a minimum value is maintained that provides tension to the cables, therefore a low load share of 10% or 5kN was chosen as the final set point. The effect of four different CFD load set points on Y drive following error performance is illustrated in **Figure 9**.

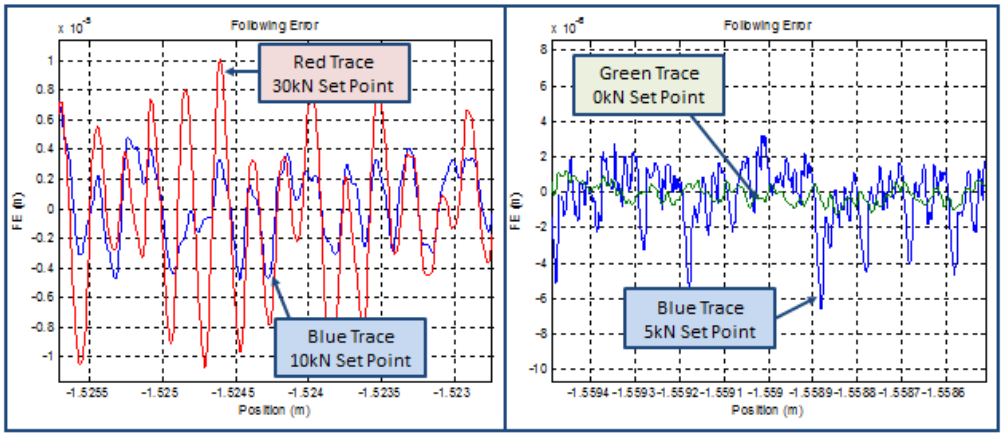

Figure 9. The Y-drive following error achieves smaller variation, increasing performance, with lower CFD set points.

3.3 System Identification

System identification models were compared against the empirical Danaher drive bode plots. The empirical bode plots were generated through response measurements during an automated frequency sweep. The goals of the models were to identify the components driving the lower frequency modes and to develop a design tool that could evaluate new drive system changes that were required to increase torque. Component FEA and catalogue stiffness values were used to accurately define the parameters in the rotational dynamic model. Given the different diameter changes along the screw the FEA models efficiently and accurately calculated the torsional stiffness of the screw with several different tracker positions, **Figure 10**.

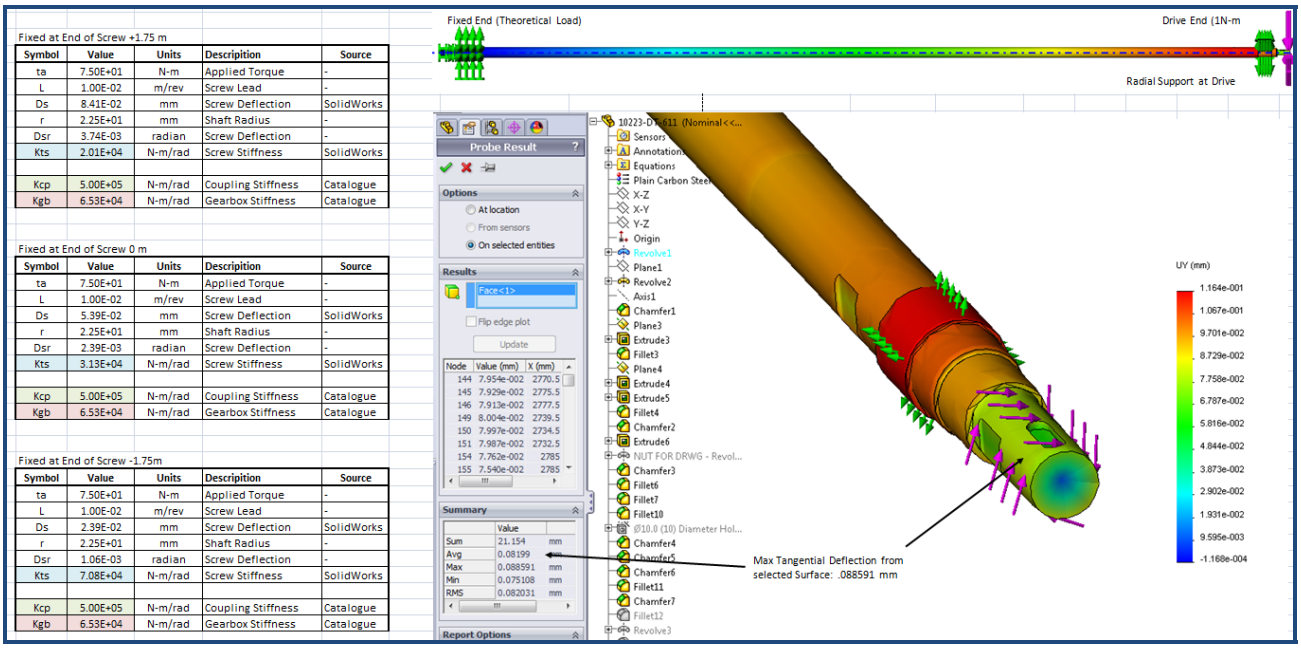

Figure 10. Stiffness parameters used for rotational dynamic model including FEA calculated torsional screw stiffness.

The transfer function defining the angular displacement of the motor to the input torque of the motor was computed using the parameters for the X and Y drive systems. The transfer function bode plots were generated using MatLab, **Figure 11**, and compared to the empirical results, **Figure 12**. The models and drives results correlated well providing validation of the calculated results. The validated models were used as a performance evaluation tool to weight changes to the drive systems to increase drive torque. Essentially, gearhead and motor changes were evaluated using the mathematical models before selections were made.

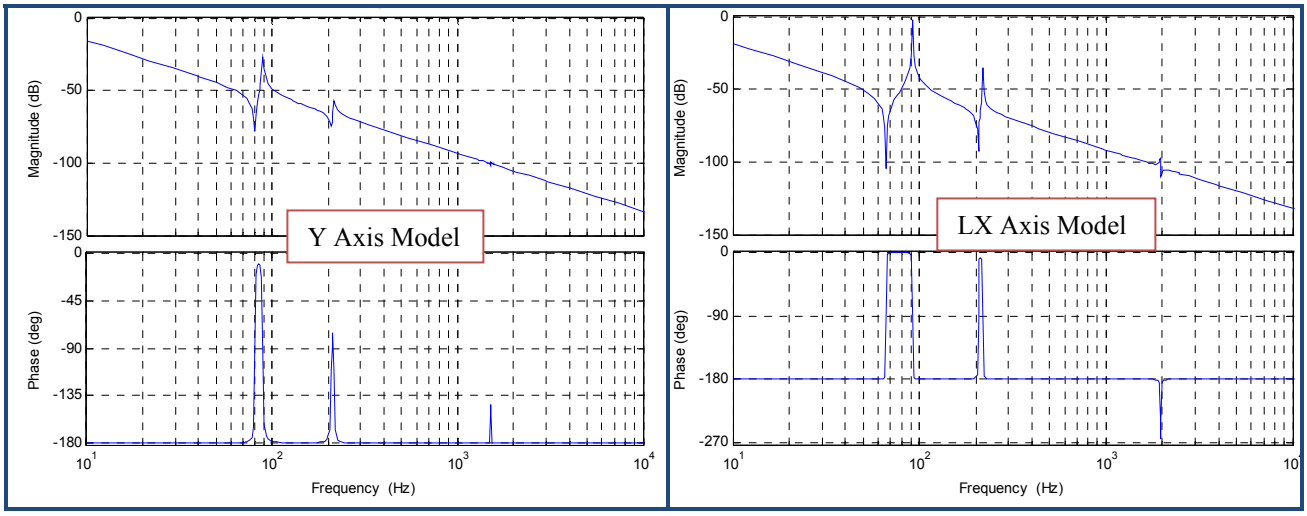

Figure 11. Y axis and LX axis bode plots generated from mathematical model of system.

Natural frequencies were recorded from the mathematical models and tabulated for comparison, **Table 1**. The Y axis evaluation cases were: case 1 – 20:1 Kollmorgen Planetary Gearhead, case 2 – 35:1 Kollmorgen Planetary Gearhead, case 3 – 100:1 Harmonic Drive Reducer. Case 1 is the validation case, but was determined to be undersized for the system torque requirements. Case 2 and Case 3 were two options for increasing the Y axes drive torque to acceptable levels. From the models it was determined that the harmonic drive system, Case 3, would yield the stiffest system, ω_1=96 Hz, however due to mechanical constraints the increase in stiffness was not substantial enough to warrant choosing the harmonic drive over the 35:1 Kollmorgen Planetary Gearhead, ω_1=81.2 Hz – Case 2.

Table 1. Evaluation list of higher torque options based on model derived natural frequencies

Y Axis Model	Parameters Reflected to Motor						Model		
	Ks (Nm/rad)	Kgb (Nm/rad)	Kc (Nm/rad)	Jgb (Kgm2)	GR	Mass (kg)	W1 (Hz)	W2 (Hz)	W3 (Hz)
Case 1	78.25	189.94	1250.00	2.60E-04	20	7711.39	89.50	214.80	1500.00
Case 2	25.55	53.32	408.16	2.50E-04	35	7711.39	81.20	203.70	1489.70
Case 3	3.13	42.00	50.00	2.10E-04	100	7711.39	96.00	337.40	1846.20
LX Axis Model	**Parameters Reflected to Motor**						**Model**		
	Ks (Nm/rad)	Kgb (Nm/rad)	Kc (Nm/rad)	Jgb (Kgm2)	GR	Mass (kg)	W1 (Hz)	W2 (Hz)	W3 (Hz)
Case 1	247.00	495.03	1100.00	9.00E-05	10	11000	92.31	218.04	1957.61
Case 2	24700.00	-	110000.00	-	-	11000	155.18	1215.94	-

The X axis evaluation cases were: case 1 – 10:1 Kollmorgen Planetary Gearhead, case 2 – no gearhead. Case 1 is the validation case and shows good correlation. From testing it was determined that Case 2 was undersized for the system torque requirements. The models indicated that no gearhead, Case 2, was the much stiffer option, ω_1=155 Hz compared to ω_1=92 Hz , but due to the need for increased torque the gearbox option, Case 1, was chosen.

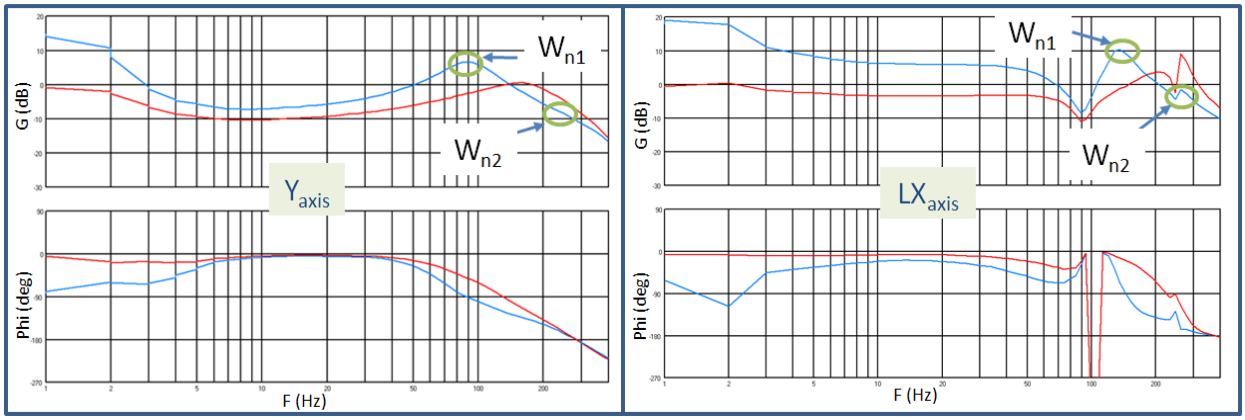

Figure 12. Empirical bode plots measured from Y and LX servo drives. The measured results correlated well to the mathematical models providing validation of the calculated model results.

The experimental bode plots show similar natural frequencies to the validation cases of from the mathematical models. The natural frequencies for the Y axis bode plot are ω_1=90 Hz and ω_2=250 Hz. The natural frequencies for the LX axis bode plot are ω_1=140 Hz and ω_2=260 Hz, **Figure 12**.

3.4 Temperature Tests

Significant viscosity changes at low temperatures were important discoveries made during testing; identifying the need for substantially higher drive torque. This was primarily a problem for the X axis since its running torque was much less than the other axes and therefore the changes at cold temperatures resulted in a significant percentage increase in the torque required by the X axis. It was determined that original screw grease viscosities reached the steep part of their exponential viscosity vs. temperature curve by 40-50°F. This was evident by the increase in drag while operating at higher speeds in colder weather. Using the original grease the slew drive reached the 3 amp maximum current at 50 mm/s for a 20°F test as compared to less than 1.5 amps at 70°F *(Figure not shown)*. After new grease was applied a 40°F test was completed that showed improvements in the viscous grease losses (i.e. losses were decreased by over 50% at 80mm/s). The slew drive could reach 80 mm/s with a 0.7 to 1.0 amp increase from the drive current required at 70°F, **Figure 13**.

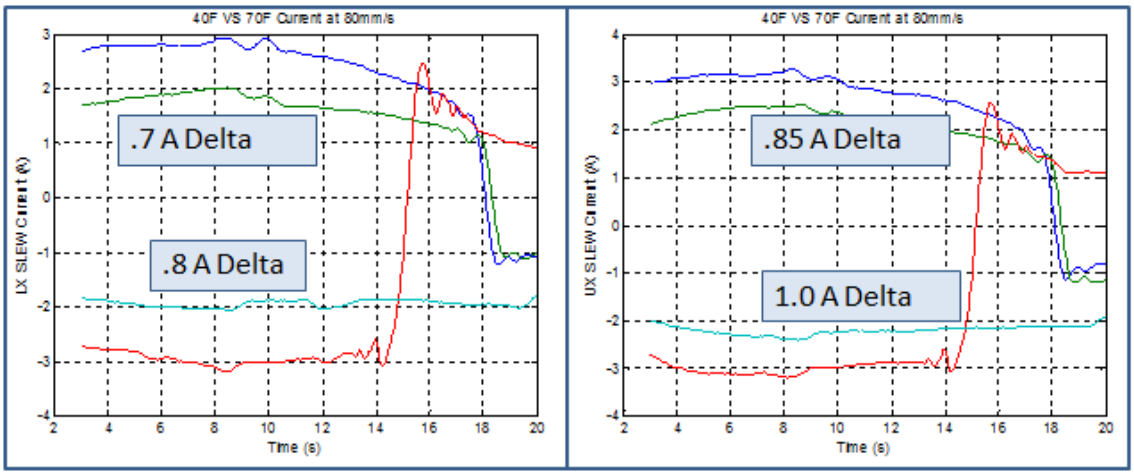

Figure 13. The increase in required drive current for LX and UX axis at 80mm/s for 70°F and 40°F ambient temperatures is shown.

4. TRACKER SYSTEM TESTING

Tracker system testing is defined as testing that occurs with the tracker in its fully assembled state. Performance was evaluated for each axis under the fully assembled configuration. Tracker system mount models were developed to compensate for structural deflection of the tracker mounting system. Future testing will include system performance testing (e.g. Open and Closed loop pointing accuracy, Tracking Accuracy, Guiding Accuracy, etc…)

4.1 Tracker System Performance Testing

The assembly of the tracker system increased payloads and resistances that resulted in adjusting control parameters to generate adequate following error performance. Sensor and control cables were installed at their full lengths, which in some cases was as long as 100 meters, to simulate the final configuration and test for increased noise and impedance problems that could develop. Large resistance forces were now in play such as the resistance from the energy chains which contained large cables and hoses that were forced to flex dynamically as the tracker moved. For the individual axes, goals of less than 10 micron RMS were targeted and testing to reach those goals is currently progressing at CEM in Austin TX.

4.2 System Mount Models

Tracker system mount models were developed to compensate for known deviations, inaccuracies, and imperfections in the mounting of the tracker system. Mount models generated for the tracker testing will be replaced once the tracker is installed at the McDonald Observatory and put into service; however for performance verification, test cell mount models were constructed. Mount models were generated for X/Y motion without hexapod movement, followed by mount models generated for hexapod motion without X/Y movement. The test setup did not include the WFC assembly, instead the WFC test mass was installed; throughout the following the SIRP location refers to a predefined point on the WFC test mass, not the actual SIRP.

Mount model generation involved superimposing the previously mapped feature locations that were measured during testing on the hexapod test stand, section 2.3, onto a few selected hexapod features locations that were measured once the hexapod was installed onto the tracker. These points generated the locations of critical geometry including the location of the SIRP relative to the Lower Hexapod Frame [LHF], which supports the hexapod.

X/Y mount models were constructed by using the laser tracker to measure the predicted location of the SIRP and the rotation of the LHF at discrete locations within travel limits. Data taken by the laser tracker was transformed into translations and rotations of the SIRP and the LHF. The measured data, compared to the commanded translations and rotations, generated errors that could be described by polynomial surface fit functions, **Figure 14**.

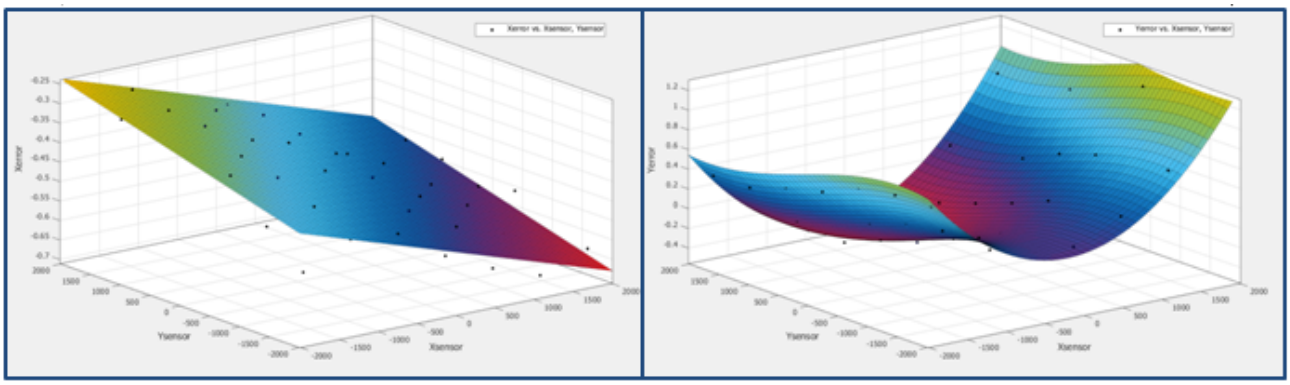

Figure 14. Error Plots with polynomial surface fits for the X and Y error of the tracker. The equations that describe the surfaces were used to generate mount model correction algorithms.

Algorithms from the polynomial surface fits were formulated and inserted into the tracker controller so that X,Y,Z, and Phi corrections were made given the command. For verification, the mount model algorithms and hexapod were activated and a reduced sampling of points was measured with the laser tracker. These points were again transformed and compared to the commands to determine the remaining error. The data comparing the error for X,Y,Z and Phi is listed in Table 2. The Mount Deflection data reflects the data sampled to create the mount models and therefore describes the deflected structure. The Mount Model Error is not zero and is a direct result of the fit error. Higher order surface polynomials would reduce this error but not substantially. The mount model does show remarkable improvements with error reduction over 90% in the Z and Phi degrees of freedom.

Table 2. The table lists the data of mount deflection and the error from the mount model. The mount model error shows considerable improvement compared to the mount deflection data.

	Xerror (mm)	Yerror (mm)	Zerror (mm)	Phi Error (ArcSec)
Maximum	-0.2615	1.2193	-4.706	160.37
Minimum	-0.6896	-0.4745	-7.847	-454
Avg	-0.4578	0.2639	-6.2933	-142.8534
RMS	0.4695	0.5139	6.3467	239.5214
STDV	0.1043	0.4409	0.8222	192.2587
Pk to Pk	0.4281	1.6938	3.141	614.37

Mount Deflection

	Xerror (mm)	Yerror (mm)	Zerror (mm)	Phi Error (ArcSec)
Maximum	0.0929	0.0924	-0.016	18.9208
Minimum	-0.1313	-0.1328	-0.2733	-30.97
Avg	0.013	0.0281	-0.1291	-1.5458
RMS	0.0496	0.0561	0.1405	11.4448
STDV	0.0478	0.0485	0.0554	11.34
Pk to Pk	0.2042	0.2252	0.2573	49.8908
Pk to Pk Impr.	0.2239	1.4686	2.8837	564.4792
% Improvement	52.30	86.70	91.81	91.88

Mount Model Error

Hexapod mount models were developed and implemented in a similar fashion. The tracker was locked at X=0, Y=0 and the hexapod was positioned within its travel limits. Measurements of the translation of the SIRP and rotation of the WFC test mass were measured with the laser tracker. Error plots were generated but algorithms have not yet been developed or implemented. Additional investigation is needed to verify that SIRP and rotation control points in the controller match the location being measured with the laser tracker. This testing is currently progressing at CEM in Austin TX.

5. SUMMARY

A multi-axis, high precision drive system has been designed and developed for the Wide Field Upgrade to the Hobby-Eberly Telescope at McDonald Observatory for initial use on the Dark Energy Experiment. A sequential laddered test approach was discussed with two parallel paths that involved hexapod testing and tracker subsystem testing.

Position control approaches were discussed while recent performance results were provided. Hexapod actuators demonstrated solid performance, less than 3 micron RMS, fully assembled. New controller methods, velocity drive control, and higher resolution feedback sensor were implemented to the X/Y axes to improve performance gains. After the changes the X/Y axes demonstrated acceptable performance at the subsystem testing level, less than 10 micron RMS, however performance roll-off started to occur during tracker testing.

Characterization measurements were illustrated and analytical methods for predicting drive dynamics and behavior were summarized. Temperature dependant test results were summarized and a reduction in viscous losses with new grease

was shown, greater than 50% reduction at 80mm/s. Performance disturbances caused by excessive CFD load share were depicted while the optimum set-point was detailed, 5kN (10%).

Structural deflection compensation methods were demonstrated at both the hexapod actuator level and the tracker testing phase. Combinations of sensor error correction and deflection prediction decreased actuator positioning error from over 40 microns to less than 5 microns. Tracker mount model corrections for the X/Y plane resulted in error reduction over 90% in the Z and Phi degrees of freedom.

Tracker testing is ongoing at CEM with further improvements being accomplished. Future testing will include system performance testing such as open and closed loop pointing accuracy, tracking accuracy, guiding accuracy, etc. These tests will also take place at the CEM test facility in Austin, TX.

REFERENCES

[1] Hill, G. J., Gebhardt, K., Komatsu, E., Drory, N., MacQueen, P. J., Adams, J. J., Blanc, G. A., Koehler, R., Rafal, M., Roth, M. M., Kelz, A., Gronwall, C., Ciardullo, R. and Schneider, D. P., "The Hobby-Eberly Telescope Dark Energy Experiment (HETDEX): Description and Early Pilot Survey Results," ASP Conf. Series, 115-118 (2008) .

[2] Hill, G. J., et al., "Current status of the Hobby-Eberly Telescope wide field upgrade", Proc. SPIE 8444-19 (2012).

[3] McDonald Observatory. (2008, January) HETDEX Illuminating the Darkness. [Online]. hetdex.org/hetdex/index.php

[4] Worthington, M. S., Beets, T. A., Good, J. M., Mock, J. R., Murphy, B. T., and South, B. J., "Design and development of a high precision, high payload telescope dual drive system", Proc. SPIE 7733, 201 (2010).

[5] Zierer, J. J., Beno, J. H., Weeks, D. A., Soukup, I. M., Good, J. M., "Design, testing, and installation of a high-precision hexapod for the Hobby-Eberly Telescope Dark Energy Experiment (HETDEX)", Proc. SPIE 8444, 176 (2012)

[6] Mock, J. R., Beno, J. H., Zierer, J. J., Rafferty, T. H., Cornell, M. E., "Tracker controls development and control architecture for the Hobby-Eberly Telescope dark energy experiment", Proc. SPIE 7733, 152 (2010)

[7] Wedeking, G. A., Zierer, J. J., Jackson, J. R., "Kinematic optimization of upgrade to the Hobby Eberly Telescope through novel use of commercially available three dimensional CAD package", Proc. SPIE 7733, 42 (2010).

[8] Mollison, N. T., Mock, J. R. Soukup, I. M., Beets, T. A., Good, J. M., Beno, J. H., Kriel, H. J., Hinze, S. E., and Wardell, D. R., "Design and development of a long-travel positioning actuator and tandem constant force actuator safety system for the Hobby-Eberly Telescope wide-field upgrade", Proc. SPIE 7733, 150 (2010).

Acknowledgement

HETDEX is run by the University of Texas at Austin McDonald Observatory and Department of Astronomy with participation from the Ludwig-Maximilians-Universität München, Max-Planck-Institut für Extraterrestriche-Physik (MPE), Leibniz-Institut für Astrophysik Potsdam (AIP), Texas A&M University, Pennsylvania State University, Institut für Astrophysik Göttingen, University of Oxford and Max-Planck-Institut für Astrophysik (MPA). In addition to Institutional support, HETDEX is funded by the National Science Foundation (grant AST-0926815), the State of Texas, the US Air Force (AFRL FA9451-04-2-0355), and generous support from private individuals and foundations.